ACS Catalysis

pubs.acs.org/acscatalysis Research Article

Operando Electrochemical Tracking of Plasmon−Photocatalytic-Coupled Cascade Catalysis in a Confined TiO_2 Nanopipette Reactor

Mei Yang, Fanwei Kong, Yanmei Ma, Shujia Wang, Tiantian Su, Junli Guo, Yan-Yan Song,* Zhida Gao,* and Junjian Zhao*

Cite This: *ACS Catal.* 2026, 16, 7611−7618 Read Online

ACCESS | Metrics & More | Article Recommendations | Supporting Information

ABSTRACT: Operando tracking of nanoscale catalytic dynamics is essential for elucidating transient interfacial events that dictate reaction efficiency. Here, we report a confined TiO_2 nanopipette reactor integrated with Au and Pt nanozymes that enables single-entity, bubble-resolved tracking of plasmon−photocatalytic-coupled cascade catalysis. Within the nanoconfined channel, glucose oxidation on Au generates H_2O_2, which is subsequently decomposed on Pt to produce periodic O_2 nanobubbles that transduce catalytic activity into well-defined ionic current oscillations. Quantitative kinetic descriptors, including the oscillation frequency, dwell time (τ_{off}), and event interval time (τ_{on}), are extracted with high reproducibility. Under 532 nm excitation, the localized surface plasmon resonance (LSPR) of Au induces hot-electron injection into TiO_2, promoting charge separation and accelerating Pt-catalyzed H_2O_2 decomposition. This coupling system enhances the O_2 generation rate while reducing both τ_{off} and τ_{on}. The nanoconfined environment enables robust catalytic detection down to 10 μM glucose, far below the macroscopic limit. Macro−micro correlated measurements further reveal synergistic regulation of the cascade kinetics by illumination and substrate concentration. This work establishes a versatile operando platform for quantifying nanoscale bubble dynamics and light-regulated cascade catalysis, offering opportunities for engineering responsive catalytic systems and next-generation microreactors.

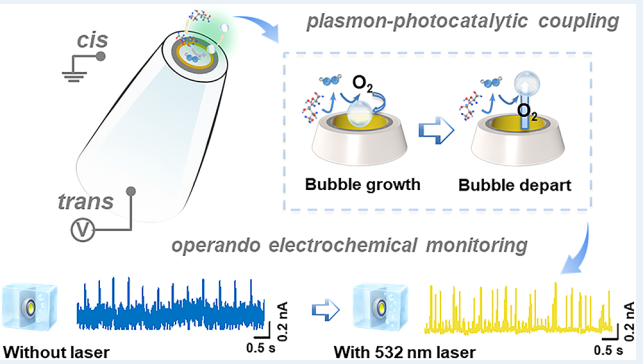

KEYWORDS: *plasmon−photocatalytic coupling, operando monitoring, TiO_2 nanopipette reactor, catalytic kinetics, bubble dynamics, cascade nanozyme reaction*

1. INTRODUCTION

Understanding catalytic reactions in real time is fundamental to advancing energy conversion, biochemical transformation, and environmental remediation technologies.[1−3] At the nanoscale, catalytic processes frequently exhibit strong spatial heterogeneity and dynamic behavior, including transient activation of interfacial sites, formation of short-lived intermediates, and local phase transitions.[4−7] Such microscopic fluctuations are often masked by ensemble-averaged measurements, underscoring the need for operando characterization platforms with high spatiotemporal resolution that can resolve catalytic events at the single-entity level.

Spectroscopic and imaging techniques have enabled in situ visualization of diverse catalytic systems,[8−12] yet challenges remain in capturing fast, localized events within confined reaction spaces or gas−liquid−solid interfaces. With rapid progress in nanopores, microelectrodes, and microfluidics, analytical methodologies have evolved toward single-entity monitoring, significantly enriching our ability to probe nanoscale dynamics.[13−18] Solid-state nanopores, in particular, offer structural robustness, label-free operation, and high sensitivity, making them powerful tools for tracking molecular transport,[19] biomolecular conformations,[20,21] biomarker analysis,[22] and interfacial processes.[23] Furthermore, the unique stability and interfacial properties of nanobubbles have positioned them as an emerging model for probing gas-involved reactions.[24] As an important model for studying gas−liquid−solid three-phase interfacial reactions, nanobubble-mediated signal transduction are integrating with nanopore devices to provide a promising avenue for studying catalytic mechanisms with unprecedented resolution.[25]

Despite these advances, quantitative operando monitoring of coupled catalytic processes involving multiple nanozymes and bubble-mediated intermediates remains challenging. Nanozymes—engineered nanomaterials with enzyme-mimicking

Received: January 19, 2026
Revised: March 6, 2026
Accepted: March 23, 2026
Published: March 26, 2026

https://doi.org/10.1021/acscatal.6c00460
ACS Catal. 2026, 16, 7611−7618

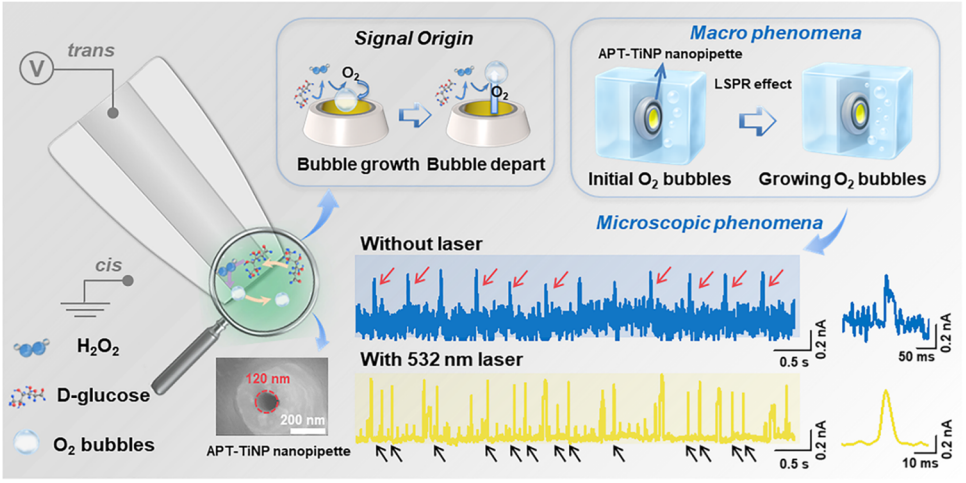

Figure 1. Schematic illustration of the APT-TiNP nanopipette measurement platform, depicting nanoscale bubble nucleation, growth, and detachment at the nanopipette orifice, together with the corresponding ionic current signatures. The comparison of current responses obtained with and without LSPR−photocatalytic coupling highlights the plasmon-enhanced acceleration of the cascade catalytic process and the resulting amplification of bubble-mediated oscillation signals.

catalytic functions—offer customizable activity, stability, and low cost, and have been widely applied in biosensing, environmental remediation, and therapeutic applications.[26−32] Multistep cascade nanozyme systems, however, introduce additional interfacial and kinetic complexities that demand precise and dynamic analytical tools. Mechanistic understanding of how external fields (e.g., photonic excitation, plasmonic hot carriers) modulate cascade pathways is especially limited.

Here, we introduce a TiO_2 nanopipette-based confined reactor that integrates Au nanozymes with glucose oxidase-mimicking activity and Pt nanozymes with catalase-mimicking activity to establish a plasmon−photocatalytic-coupled cascade system. Within this nanoscale geometry, glucose oxidation generates H_2O_2, followed by Pt-catalyzed decomposition into O_2 nanobubbles. The formation, growth, and detachment of these bubbles produce characteristic ionic current oscillations, enabling conversion of catalytic events into quantifiable single-channel electrical signals (Figure 1). By analyzing dwell time (τ_{off}) of nanobubbles, we resolve the reaction kinetics with high fidelity. Importantly, excitation of Au localized surface plasmon resonance (LSPR) at 532 nm induces hot-electron injection into TiO_2, facilitating charge separation and significantly accelerating the cascade reaction. The synergistic LSPR−photocatalytic effect boosts the O_2 generation rate more than 4-fold (comparing the O_2 generation rate at 130 $mW{\cdot}cm^{-2}$ to 0 $mW{\cdot}cm^{-2}$). Correlated macro−micro experiments validate that both illumination intensity and substrate concentration cooperatively regulate the cascade kinetics. Notably, the confined nanopipette environment supports highly reactive catalytic behavior even at glucose concentrations as low as 10 μM—levels undetectable macroscopically. This work establishes a generalizable operando platform for resolving nanoscale bubble dynamics and light-regulated cascade catalysis. Beyond offering mechanistic insights into nanozyme systems, this approach provides a blueprint for developing intelligent, responsive catalytic microreactors and functional materials tailored for energy and biochemical transformations.

2. EXPERIMENTAL SECTION

2.1. Chemicals and Reagents

Foils (0.02 mm thick, 99.6% purity) were purchased from Baosheng Hardware. Sodium borohydride ($NaBH_4$) was obtained from Aladdin. Glucose (Glu) and tris(hydroxymethyl)aminomethane (Tris) were purchased from Sigma-Aldrich. Ethylene glycol, ammonium fluoride (NH_4F), triethylene glycol (TEG), chloroauric acid trihydrate ($HAuCl_4{\cdot}3H_2O$), hexachloroplatinic acid hexahydrate ($H_2PtCl_6{\cdot}6H_2O$), hydrochloric acid, sodium dodecyl sulfate (SDS), hydrogen peroxide (H_2O_2), and all other chemicals were supplied by Sinopharm Chemical Reagent Co., Ltd. All reagents were of analytical grade and used as received without further purification.

2.2. Preparation of APT-TiNP Arrays

TiO_2 nanopipette arrays (TiNPs) were fabricated following the anodization procedure reported by Schmuki and co-workers.[33] TiO_2 nanoparticles were subsequently deposited at the tube openings to achieve pore shrinking, and the samples were annealed at 300 °C for 2 h to obtain TiO_2−TiNPs (T-TiNPs). Pt/TiO_2−TiNPs (PT-TiNPs) were prepared according to a previously reported reduction method.[34] Briefly, T-TiNPs were immersed in 10 mL of a 2 mM H_2PtCl_6 aqueous solution, followed by the addition of 0.5 mL of 50 mM sodium citrate. Under vigorous stirring, 1.17 mL of 120 mM $NaBH_4$ was introduced, and the reaction was allowed to proceed for 40 min. The resulting PT-TiNPs were then incubated in 1 mM $HAuCl_4$ at 70 °C for 2 h. After thorough washing with deionized water, the samples were immersed in 0.1 mM $NaBH_4$ for 15 min to reduce Au^{3+}, yielding Au/Pt/TiO_2−TiNPs (APT-TiNPs).[35]

2.3. Preparation of Individual Nanopipette

To obtain individual nanopipette, 2 μL of a hexane solution containing PDMS (prepolymer/curing agent = 10:1 by mass) was infiltrated into the intertube gaps of APT-TiNPs.[36] The samples were dried at 70 °C for 2 h to allow PDMS infiltration and solidification, forming a detachable PDMS film. Peeling the film produced isolated APT-TiNP nanopipette, which were subsequently mounted onto PDMS gaskets with 1 μm pores for measurements.

2.4. Electrochemical Testing

Ion current measurements were conducted using a nanopipette-based electrochemical platform. A single nanopipette was positioned between two Teflon chambers filled with electrolyte solutions. One chamber contained Tris−HCl buffer (10 mM Tris−HCl, 10 mM KCl, 0.5 wt % SDS, pH 7.4), while the other contained the same buffer supplemented with glucose. Time-resolved ionic current recordings

https://doi.org/10.1021/acscatal.6c00460
ACS Catal. 2026, 16, 7611−7618

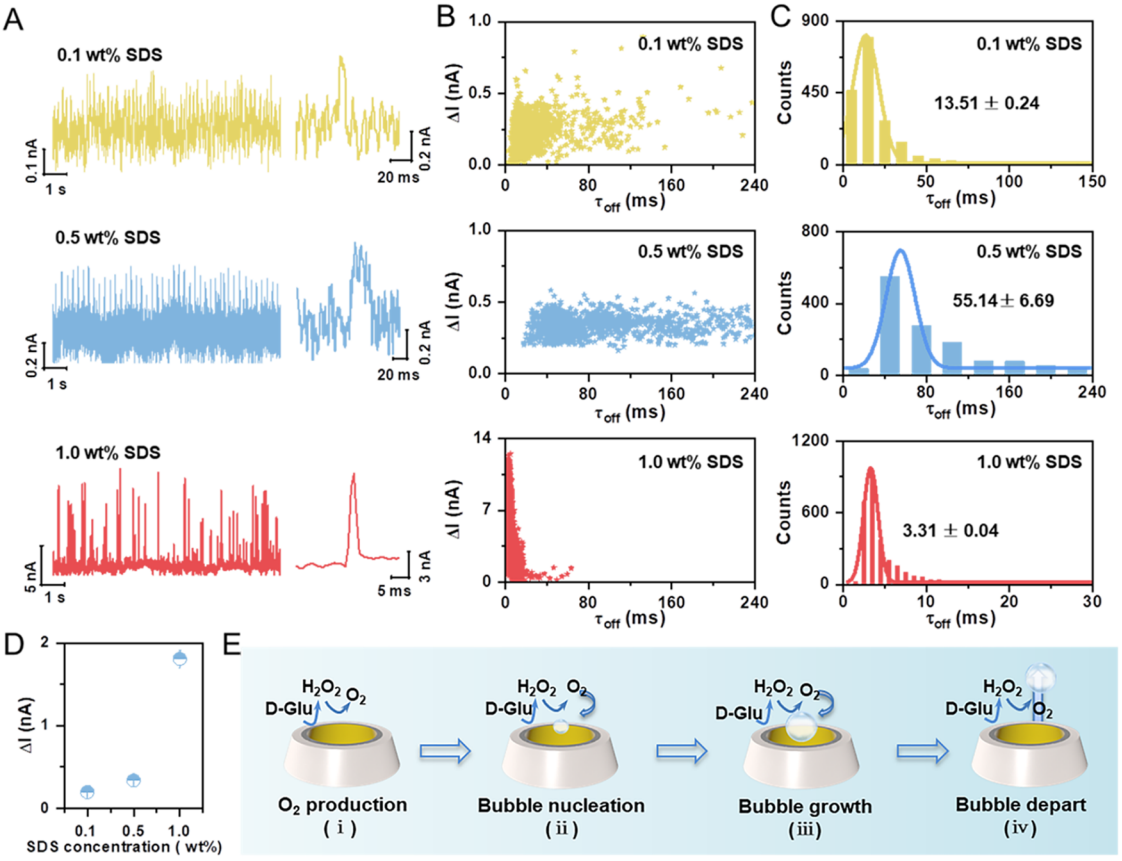

Figure 2. Characterization of SDS-regulated bubble dynamics in an APT-TiNP nanopipette. (A) Representative ionic current−time traces showing periodic oscillations induced by O_2 nanobubble formation and detachment at varying SDS concentrations. (B) Corresponding scatter plots mapping the distribution of bubble-related current events. (C) Histograms of bubble τ_{off} revealing SDS-dependent modulation of bubble stability. (D) Trend of current amplitude (ΔI) as a function of SDS concentration. (E) Schematic illustration of the nucleation, growth, and detachment processes of O_2 bubbles at the nanopipette orifice. Number of individual experiments, n = 3.

were obtained under constant applied voltage using an eONE Plus data acquisition system (Elements, Italy) at a sampling rate of 1.25 kHz. Ag/AgCl electrodes were used in all measurements. For all experiments, the working electrode was placed on the buffer-only side, and a positive bias was applied to drive ion transport toward the nanopipette orifice.

2.5. Data Analysis

All ionic current traces were processed and analyzed using Clampfit 11.2 (Molecular Devices, USA). Statistical analyses, distribution plots, and graphical outputs were generated using OriginLab 2022 (OriginLab Corporation, USA).

3. RESULTS AND DISCUSSION

3.1. Preparation and Characterization of Nanopipette

Vertically aligned TiO_2 nanopipette arrays (TiNPs) were fabricated via anodic oxidation, producing tubes with diameters of ∼200 nm, lengths of ∼6.1 μm, and intertube spacing of 300 ± 50 nm (Figure S1). To improve sensitivity toward bubble-mediated ionic current modulation, $TiCl_4$ hydrolysis was employed to deposit TiO_2 nanoparticles within the tubes, reducing their inner diameter to ∼130 ± 10 nm (Figure S2) and yielding anatase TiO_2 after an annealing treatment at 300 °C for 2 h.[37] Subsequent chemical reduction deposited Pt and Au nanoparticles onto the inner and outer tube walls (Figure S3), forming Au/Pt/TiO_2−TiNPs (APT-TiNPs). TEM, HRTEM, and EDS analyses (Figure S4) confirmed uniform nanoparticle distribution, while XRD patterns validated the crystalline phases of TiO_2, Pt, and Au (Figure S5). Zeta potential measurements revealed increased negative charge following Pt and Au modification, favoring enhanced ionic interactions (Figure S6). Embedding the APT-TiNP arrays in PDMS and peeling yielded individual nanopipette with 120 ± 4 nm openings (Figure S7). I−V characteristics of TiNP and APT-TiNP nanopipette were tested (Figure S8). As APT was modified onto the surface of individual TiNP, the recorded ion current in 0.01 M KCl solution gradually decreased. The change in ion current can be attributed to the steric hindrance effect introduced by the APT modification. Additionally, to assess sample-to-sample reproducibility, nine independently fabricated APT-TiNP nanopipette prepared under identical conditions were used for ionic current measurements. The baseline current (I_0) exhibited a relative standard deviation (RSD) of 8.01%, indicating the good consistency among independently prepared samples (Figure S9). The APT-TiNP provides a stable material basis and an in situ nanopipette monitoring system for subsequent studies on the kinetics of glucose catalytic oxidation.

3.2. Bubble-Mediated Cascade Reaction Mechanism

In the cascade process, Au nanozymes catalyze glucose oxidation to produce H_2O_2, which is subsequently decomposed into O_2 on Pt. The generated O_2 nanobubbles can be captured as oscillatory ionic current signals (I−t) under an applied bias on the Ag/AgCl electrode, enabling real-time tracking of catalytic kinetics. In the nanopipette system, two

https://doi.org/10.1021/acscatal.6c00460
ACS Catal. 2026, 16, 7611−7618

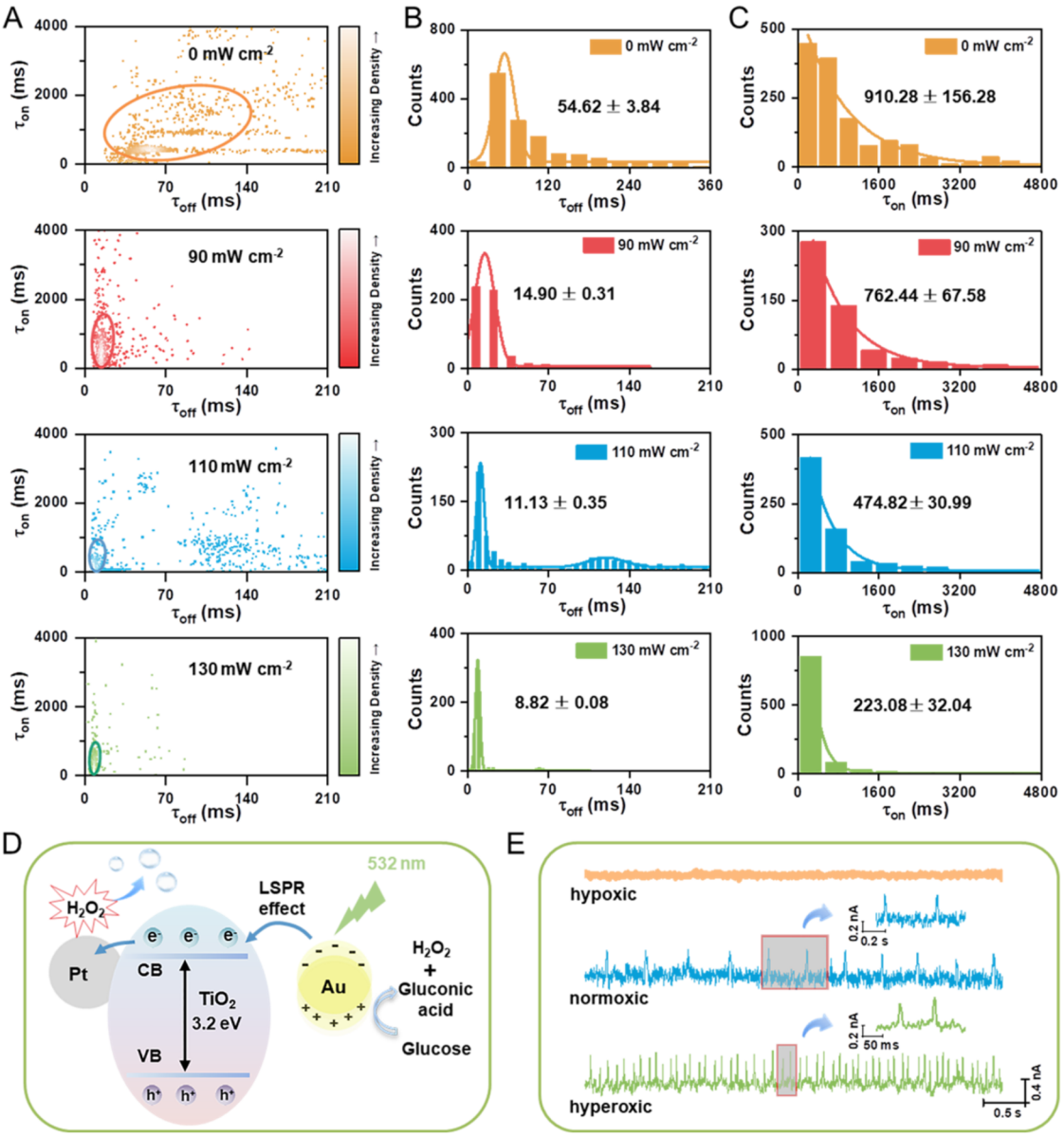

Figure 3. Photocatalytic modulation of cascade reaction kinetics in an APT-TiNP nanopipette under LSPR excitation. (A) Density scatter plots of ionic current events recorded at different laser powers, illustrating the acceleration of bubble-mediated catalytic turnover. (B) Histogram distributions of bubble τ_{off} and (C) τ_{on}, showing progressively shortened kinetic parameters with increasing illumination intensity. (D) Schematic illustration of the LSPR-induced enhancement mechanism, highlighting hot-carrier generation, charge separation, and accelerated H_2O_2 decomposition in the Au/TiO_2/Pt cascade system. (E) Representative current−time traces collected under hypoxic, normoxic, and hyperoxic conditions, demonstrating the influence of dissolved oxygen on cascade reaction dynamics. Number of individual experiments, n = 3.

parameters—current amplitude (ΔI) and bubble dwell time (τ_{off})—directly reflect the physicochemical behavior of nanobubbles at the orifice. However, in 10 mM glucose buffer without additives, no discernible current modulation is detected (Figure S10), likely due to (i) rapid formation of relatively large bubbles and (ii) their strong adhesion to the surface, which obstructs ion transport and suppresses signal formation. To address this limitation, an anionic surfactant, sodium dodecyl sulfate (SDS), was introduced to modulate bubble nucleation and detachment. Owing to their amphiphilic nature, SDS molecules preferentially adsorb at the bubble−liquid interface, lowering interfacial tension and facilitating the formation of smaller, more mobile bubbles.[38] Upon SDS addition, periodic oscillatory signals with well-defined amplitudes emerge (Figure 2A). Statistical analyses of scatter plots (Figure 2B), τ_{off} distributions (Figure 2C), and the trend of current amplitude changes at varying SDS concentrations (Figures 2D and S11) reveal that ΔI increases monotonically with SDS concentration, whereas τ_{off} exhibits a nonmonotonic trend—first increasing and then decreasing. This behavior reflects the dual regulatory role of SDS on bubble nucleation and growth, consistent with classical nucleation theory, in which bubble formation proceeds through nucleation followed by growth.[39,40] Based on the above experimental observations, the bubble evolution process at the nanopipette opening can be described in four stages (Figure 2E):

(i) Supersaturation: Continuous generation of O_2 molecules via cascade reactions, which increases local concentration until supersaturation is reached.

https://doi.org/10.1021/acscatal.6c00460
ACS Catal. 2026, 16, 7611−7618

(ii) Nucleation: O_2 nuclei form at the nanopipette opening once a critical concentration is exceeded.

(iii) Growth with SDS adsorption: As bubbles grow, SDS molecules accumulate at the interface, orienting their hydrophobic tails inward and their negatively charged heads outward. This results in negatively charged nanovesicle-like structures that enhance local ion enrichment, thereby increasing the ion current.

(iv) Detachment: When bubbles reach a critical size, electrostatic repulsion and buoyancy drive their detachment, yielding the observed pulse-like current signals.

The amplitude enhancement with increasing SDS concentration (Figure 2D) is attributed to stronger interfacial adsorption and improved ion accumulation. Meanwhile, the τ_{off} increases and then decreases with increasing SDS concentration (Figure 2C). This behavior may be attributed to the SDS-mediated suppression of Ostwald ripening at moderate concentrations and micelle-induced repulsion at higher concentrations,[41] which promotes the faster detachment of the bubbles from the openings, thereby shortening τ_{off}. Optical microscopy images of Pt-catalyzed H_2O_2 decomposition (Figure S12) further corroborate the modulatory effect of SDS on bubble morphology and dynamics.

To further optimize nanobubble detection, the applied bias voltage was investigated (Figure S13). Increasing the voltage from 400 to 600 mV significantly shortens τ_{off} (from 88.50 to 26.00 ms), consistent with enhanced electroosmotic flow driving negatively charged bubbles away from the nanopipette orifice. A potential of 500 mV was selected for subsequent experiments as a balance between signal clarity and system stability. Furthermore, control experiments establish that the observed oscillations originate exclusively from O_2 nanobubbles generated during the cascade reaction. No signal is detected for APT-TiNP in SDS-only buffer (Figure S14), nor for AT-TiNP in glucose solution (Figure S15). However, PT-TiNP in H_2O_2 solution yield clear periodic signals (Figure S16), confirming the catalytic decomposition of H_2O_2 on Pt as the direct source of O_2 bubble formation. The gas pressure experiment further confirmed that SDS primarily regulates bubble dynamics without affecting the intrinsic catalytic activity of gold and platinum nanozymes (Figure S17). These results demonstrate that time-resolved ionic current oscillations provide a robust, quantitative readout of nanobubble dynamics and thus of the underlying cascade catalytic kinetics.

3.3. LSPR−Photocatalytic Coupling Modulates Catalytic Behavior

Light serves as an important physical stimulus for regulating nanoscale catalytic processes. UV−vis absorption spectra reveal that the AuNPs exhibit a distinct LSPR peak at 523 nm (Figure S18), while the solid-state spectrum of APT-TiNPs shows enhanced visible-light absorption arising from the plasmonic component (Figure S19). Guided by this spectral character, a 532 nm laser was employed to probe how LSPR influences the cascade catalytic reaction. The corresponding $I-t$ traces under illumination demonstrate a marked increase in the frequency and sharpness of oscillatory features associated with O_2 nanobubble formation (Figure S20). To quantitatively assess catalytic performance, the bubble τ_{off} and event interval time (τ_{on}) were extracted as kinetic descriptors, with the inverse of τ_{on} representing the O_2 generation rate r_{on} (Supporting Note 1).[42] Statistical analyses—including density scatter plots (Figure 3A), dwell-time histograms (Figure 3B), and event-interval-time histograms (Figure 3C) show that both τ_{off} and τ_{on} decrease monotonically with increasing laser intensity. Specifically, τ_{off} decreases from 54.62 ms (0 mW cm^{-2}) to 8.82 ms (130 mW cm^{-2}), while r_{on} increases from 1.10 s^{-1} (dark) to 1.31 s^{-1} (90 mW cm^{-2}), 2.11 s^{-1} (110 mW cm^{-2}), and 4.48 s^{-1} (130 mW cm^{-2}). At the maximum illumination available, the O_2 generation rate increases by a factor of ∼4.1, demonstrating that the integration of Au-LSPR with the photocatalytic properties of TiO_2 markedly accelerates the cascade catalytic reactions.

To clarify the origin of this enhancement, infrared thermography was used to monitor the temperature of APT-TiNPs under illumination. The temperature increase remained below 5 °C (Figure S21), indicating negligible photothermal contribution. Thus, the observed acceleration is attributed primarily to plasmon-induced charge processes rather than heating. In this case, AuNPs with GOx-mimicking activity catalyze glucose oxidation to H_2O_2 in the dark,[43,44] while PtNPs with CAT-mimicking activity decompose H_2O_2 to O_2.[45] Furthermore, the current−time measurements at different laser wavelengths (380, 405, 532, 638, and 785 nm) under the same power density (130 mW cm^{-2}) confirm that 532 nm-laser yields the highest O_2 generation rate, thus supporting the key role Au-LSPR effect in this system (Figures S22 and S23). As illustrated in Figure 3D, under visible-light irradiation, LSPR excitation generates hot electrons and hot holes in AuNPs.[46] The hot holes participate directly in glucose oxidation, whereas hot electrons are injected into the TiO_2 conduction band due to favorable band alignment and subsequently transferred to Pt, where they accelerate H_2O_2 decomposition.[47]

This plasmon−photocatalytic coupling promotes efficient electron−hole separation and substantially boosts both steps of the cascade reaction. Because the cascade process simultaneously consumes O_2 (Au-mediated oxidation) and produces O_2 (Pt-mediated decomposition), its performance is intrinsically sensitive to dissolved oxygen levels. Experiments conducted under hypoxic, normoxic, and hyperoxic conditions (Figures 3E and S24). The results reveal that O_2 generation and consumption within the system can be dynamically regulated, maintaining efficient catalytic turnover under physiological oxygen levels. These observations underscore the robustness of the APT-TiNP confined reactor and highlight the strong external-field responsiveness of the nanozyme cascade. These results demonstrate that LSPR−photocatalytic coupling serves as an effective strategy to modulate nanoscale cascade catalysis with high precision, enabling significant enhancement of enzyme-free glucose oxidation under mild conditions. This light-responsive catalytic platform offers mechanistic insights and design principles that can be leveraged in developing intelligent, energy-efficient catalytic systems and next-generation photoelectrochemical microreactors.

3.4. Macro−Micro Comparison of Catalytic Performance

To evaluate whether operando nanobubble monitoring can elucidate factors governing macroscopic catalytic behavior, the kinetic parameters obtained from single-nanopipette measurements were systematically compared with those from bulk APT-TiNP arrays. The effects of light intensity and substrate concentration were examined in both macroscopic reactors (1 cm diameter APT-TiNP arrays) and individual nanopipette. At the macroscopic scale, oxygen evolution was quantified in real

https://doi.org/10.1021/acscatal.6c00460
ACS Catal. 2026, 16, 7611−7618

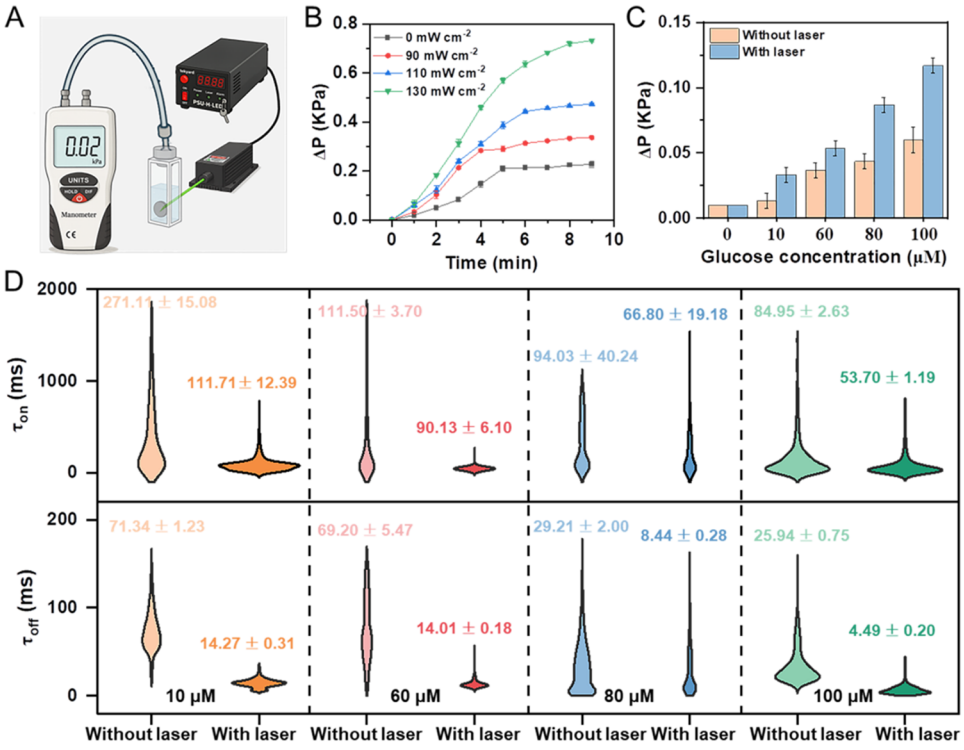

Figure 4. Macro−micro correlation of cascade catalytic performance in APT-TiNP systems. (A) Schematic illustration for measuring O_2 generation from glucose via the Au/Pt nanozyme cascade on APT-TiNPs. (B) Pressure−time curves showing macroscopic O_2 evolution from 1 mM glucose under varying laser powers, demonstrating LSPR-enhanced catalytic activity. Error bars represent standard deviations from three independent experiments (n = 3). (C) Pressure changes associated with O_2 production at different glucose concentrations, with and without illumination, highlighting the synergistic effects of substrate availability and light excitation. Error bars represent standard deviations from three independent experiments (n = 3). (D) Violin plots of bubble τ_{off} and τ_{on} obtained from single-nanopipette measurements, revealing accelerated and more uniform catalytic kinetics at higher glucose concentrations and under illumination. Number of individual experiments, n = 3.

time by monitoring pressure changes ($\Delta P = P - P_0$) in a sealed chamber using a digital differential manometer (Figure 4A). As laser power increased, ΔP rose proportionally (Figure 4B), consistent with LSPR-enhanced catalytic activity observed at the microscale (Figure 3). Similarly, glucose concentration exhibited a positive correlation with pressure changes over a 9 min reaction period. Under LSPR−photocatalytic coupling, glucose oxidation proceeded more rapidly, resulting in significantly amplified pressure signals (Figures 4C and S25).

At the microscale, I−t traces were recorded for individual APT-TiNP nanopipette in glucose solutions of varying concentration under both dark conditions (Figure S26) and illumination at 110 mW cm^{-2} (Figure S27). Statistical analysis of the extracted bubble parameters produced violin plots (Figure 4D) and distribution histograms (Figures S28 and S29). Both τ_{off} and τ_{on} decreased monotonically with increasing glucose concentration, indicating accelerated bubble formation. Notably, illumination further reduced these parameters while narrowing their distributions, demonstrating more rapid and uniform catalytic turnover. These results corroborate the strong synergistic regulation of cascade kinetics by LSPR excitation and substrate availability. Strikingly, at glucose concentrations as low as 10 μM, macroscopic reactors produced virtually no measurable oxygen, whereas the nanopipette system exhibited clear oscillatory signals corresponding to an O_2 generation rate of 3.69 s^{-1} (Table S1). This dramatic contrast highlights the superior reactivity enabled by nanoscale confinement, where restricted diffusion, enhanced local enrichment, and intensified electric fields collectively sustain efficient catalysis even under dilute conditions. The above macro−micro comparison reveals a unified kinetic picture: Substrate concentration and illumination act cooperatively across scales, but confinement dramatically amplifies catalytic responsiveness. These findings underscore the importance of geometry-engineered microenvironments in modulating cascade nanozyme reactions and provide a mechanistic basis for designing highly sensitive, controllable, and light-responsive nanocatalytic platforms.

4. CONCLUSION

In conclusion, we developed a confined TiO_2 nanopipette reactor that enables operando, single-entity tracking of plasmon−photocatalytic cascade catalysis directly at the reaction site with high sensitivity and mechanistic precision. By integrating Au and Pt nanozymes within the nanoscale pipet and regulating bubble nucleation and detachment through SDS, well-defined ionic oscillations are obtained, from which quantitative kinetic descriptors (τ_{off} and τ_{on}) are reliably extracted. Under 532 nm excitation, Au-LSPR−induced hot-electron injection into TiO_2 markedly accelerates both glucose oxidation and H_2O_2 decomposition, enhancing the O_2 generation rate by more than 4-fold (comparing the O_2 generation rate at 130 mW·cm^{-2} to 0 mW·cm^{-2}) and amplifying the electrochemical readout of catalytic events. Macro−micro correlated studies further reveal that illumination and substrate concentration synergistically regulate cascade kinetics, while nanoscale confinement enables robust detection at glucose concentrations far below macroscopic

https://doi.org/10.1021/acscatal.6c00460
ACS Catal. 2026, 16, 7611−7618

limits. The confined TiO_2 nanopipette reactor transduces O_2 nanobubble formation into directly readable ionic oscillations with single-entity sensitivity, enabling quantitative analysis of nanozyme activity and catalytic kinetics at the nanoscale. This work establishes a versatile operando platform for resolving nanoscale bubble dynamics and light-regulated cascade catalysis.

■ ASSOCIATED CONTENT

Supporting Information

The Supporting Information is available free of charge at https://pubs.acs.org/doi/10.1021/acscatal.6c00460.

Fabrication procedure of APT-TiNPs; SEM images of spaced TiO_2 nanopipette arrays, T-TiNPs, and the APT-TiNP nanopipette; TEM, HRTEM, and EDS elemental mapping of APT-TiNPs; XRD patterns of TiNPs, PT-TiNPs, and APT-TiNPs; zeta potential distributions; *I*−*V* curves of TiNP and APT-TiNP nanopipettes; typical current−time traces of APT-TiNP, AT-TiNP, and PT-TiNP nanopipettes in various buffer solutions; UV−vis absorption spectrum of AuNPs and diffuse reflectance spectra of TiNPs and APT-TiNPs; optical images of O_2 bubble generation; infrared thermal images under laser irradiation; time-dependent pressure variation curves; and oxygen generation rates under macroscopic and microscopic conditions (PDF)

■ AUTHOR INFORMATION

Corresponding Authors

Yan-Yan Song − *College of Sciences, Northeastern University, Shenyang 110819, P. R. China*; orcid.org/0000-0001-5150-4784; Email: yysong@mail.neu.edu.cn

Zhida Gao − *College of Sciences, Northeastern University, Shenyang 110819, P. R. China*; orcid.org/0000-0002-9804-8170; Email: gaozd@mail.neu.edu.cn

Junjian Zhao − *Department of Pharmacy, Shenyang Medical College, Shenyang 110034, P. R. China*; Email: jjzhao@symc.edu.cn

Authors

Mei Yang − *College of Sciences, Northeastern University, Shenyang 110819, P. R. China*

Fanwei Kong − *College of Sciences, Northeastern University, Shenyang 110819, P. R. China*

Yanmei Ma − *College of Sciences, Northeastern University, Shenyang 110819, P. R. China*

Shujia Wang − *College of Sciences, Northeastern University, Shenyang 110819, P. R. China*

Tiantian Su − *College of Sciences, Northeastern University, Shenyang 110819, P. R. China*

Junli Guo − *College of Sciences, Northeastern University, Shenyang 110819, P. R. China*

Complete contact information is available at: https://pubs.acs.org/10.1021/acscatal.6c00460

Author Contributions

Y.-Y. Song conceived the concept and directed the project. M.Y., F.W.K., Y.M.M., S.J.W., T.T.S. and J.L.G. performed the experiments. Z.D.G. and J.J.Z. collected and analyzed the data. M.Y. prepared the first draft of this manuscript, and all the authors modified the manuscript.

Notes

The authors declare no competing financial interest.

■ ACKNOWLEDGMENTS

This work was supported by the National Natural Science Foundation of China, China (No. 22374015); Liaoning Province Foundation for Distinguished Young Scholars, China (No. 2024JH3/50100012, to Y.−Y.S.); Fundamental Research Funds for the Central Universities, China (N25QNR014 and N2424020); The PhD Start-up Foundation of Liaoning Province, China (No. 2025-BS-0868). Special thanks are due to the instrumental or data analysis from the Analytical and Testing Center, Northeastern University.

■ REFERENCES

(1) Huang, Y.; Mou, C.; Liang, J.; Wan, J.; Chen, P.; Guan, B.-O. Operando decoding of surface chemical and thermal events in photoelectrocatalysis via a lab-around-microfiber sensor. *Adv. Sci.* **2024**, *11* (26), No. 2310264.

(2) Kwon, H.; Choi, H.; Yoon, Y.; Jeon, B.; Kang, M.; Park, J. Y.; Kim, H. Y.; Lee, S. W. Electronic switching between hot electrons and hot holes via schottky junctions during chemical reactions. *ACS Nano* **2025**, *19* (11), 11450−11462.

(3) Wang, R.; Yang, X.; Zhang, J.; Wen, S.; Yan, L.; Zhao, X.; Guo, E. In-situ characterization technologies and theoretical calculations in carbon dioxide reduction: In-depth understanding of reaction mechanisms and rational design of electrocatalysts. *Coord. Chem. Rev.* **2025**, *533*, No. 216541.

(4) Cuenya, B. R.; Bañares, M. A. Introduction: Operando and in situ studies in catalysis and electrocatalysis. *Chem. Rev.* **2024**, *124* (13), 8011−8013.

(5) Yu, D.; Garcia, A. I. V.; Blum, S. A.; Welsher, K. D. Growth kinetics of single polymer particles in solution via active-feedback 3D tracking. *J. Am. Chem. Soc.* **2022**, *144* (32), 14698−14705.

(6) Yang, L.; Feng, J.; Wang, J.-N.; Gao, Z.; Xu, J.; Mei, Y.; Song, Y.-Y. Engineering large-scaled electrochromic semiconductor films as reproductive SERS substrates for operando investigation at the solid/liquid interfaces. *Chin. Chem. Lett.* **2022**, *33* (12), 5169−5173.

(7) DeJong, M.; Price, A. J. A.; Mårsell, E.; Tom, G.; Nguyen, G. D.; Johnson, E. R.; Burke, S. A. Small molecule binding to surface-supported single-site transition-metal reaction centres. *Nat. Commun.* **2022**, *13* (1), No. 7407.

(8) He, Y.; Liu, S.; Wang, M.; Cheng, Q.; Ji, H.; Qian, T.; Yan, C. Advanced in situ characterization techniques for direct observation of gas-involved electrochemical reactions. *Energy Environ. Mater.* **2023**, *6* (6), No. e12552.

(9) Xu, J.; Liang, C.; Gao, Z.; Song, Y.-Y. Construction of nanoreactors on TiO_2 nanotube arrays as a POCT device for sensitive colorimetric detection. *Chin. Chem. Lett.* **2023**, *34* (5), No. 107863.

(10) Liu, X.; Chen, J.; Wei, Z.; Yi, H.; Lei, A. Deciphering reactive intermediates in electrooxidative coupling of indoles through real-time mass spectrometry. *Chem* **2024**, *10* (7), 2131−2146.

(11) Liu, R.; He, Z.; Sun, J.; Liu, J.; Jiang, G. Tracking the fate of surface plasmon resonance-generated hot electrons by in situ sers surveying of catalyzed reaction. *Small* **2016**, *12* (46), 6378−6387.

(12) Shen, T.-H.; Girod, R.; Tileli, V. Insights into electrocatalyst transformations studied in real time with electrochemical liquid-phase transmission electron microscopy. *Acc. Chem. Res.* **2023**, *56* (21), 3023−3032.

(13) Balogun, Y.; Yang, R.; Wang, G. Resistive pulse sensing of pre-nucleation activities during single-entity lysozyme crystallization on single nanopipettes. *Sens. Actuators Rep.* **2025**, *9*, No. 100281.

(14) Li, Z.-Q.; Huang, L.-Q.; Wang, K.; Xia, X.-H. Developing solid-state single-, arrayed-, and composite-nanopore sensors for bio-chemical sensing applications. *Acc. Mater. Res.* **2024**, *5* (6), 761−771.

(15) Lee, J.; Kang, Y.; Chang, J.; Song, J.; Kim, B.-K. Determination of serotonin concentration in single human platelets through single-entity electrochemistry. *ACS Sens.* **2020**, *5* (7), 1943−1948.
(16) Defnet, P. A.; Zhang, B. Collision, adhesion, and oxidation of single ag nanoparticles on a polysulfide-modified microelectrode. *J. Am. Chem. Soc.* **2021**, *143* (39), 16154−16162.
(17) Ma, W.; Ma, H.; Peng, Y.-Y.; Tian, H.; Long, Y.-T. An ultrasensitive photoelectrochemical platform for quantifying photo-induced electron-transfer properties of a single entity. *Nat. Protoc.* **2019**, *14* (9), 2672−2690.
(18) Wu, Z.; Zheng, Y.; Lin, L.; Xing, G.; Xie, T.; Lin, J.; Wang, X.; Lin, J.-M. Construction of multiplexed assays on single anisotropic particles using microfluidics. *ACS Cent. Sci.* **2025**, *11* (2), 294−301.
(19) Li, M.-Y.; Jiang, J.; Li, J.-G.; Niu, H.; Ying, Y.-L.; Tian, R.; Long, Y.-T. Nanopore approaches for single-molecule temporal omics: Promises and challenges. *Nat. Methods* **2025**, *22* (2), 241−253.
(20) Ma, H.; Wang, Y.; Li, Y.-X.; Xie, B.-K.; Hu, Z.-L.; Yu, R.-J.; Long, Y.-T.; Ying, Y.-L. Label-free mapping of multivalent binding pathways with ligand−receptor-anchored nanopores. *J. Am. Chem. Soc.* **2024**, *146* (41), 28014−28022.
(21) Galenkamp, N. S.; Biesemans, A.; Maglia, G. Directional conformer exchange in dihydrofolate reductase revealed by single-molecule nanopore recordings. *Nat. Chem.* **2020**, *12* (5), 481−488.
(22) Tang, H.; Wang, H.; Zhao, D.; Cao, M.; Zhu, Y.; Li, Y. Nanopore-based single-entity electrochemistry for the label-free monitoring of single-molecule glycoprotein−boronate affinity interaction and its sensing application. *Anal. Chem.* **2022**, *94* (14), 5715−5722.
(23) Tsutsui, M.; Hsu, W.-L.; Hsu, C.; Garoli, D.; Weng, S.; Daiguji, H.; Kawai, T. Transmembrane voltage-gated nanopores controlled by electrically tunable in-pore chemistry. *Nat. Commun.* **2025**, *16* (1), No. 1089.
(24) Hu, Y.-X.; Ying, Y.-L.; Gao, R.; Yu, R.-J.; Long, Y.-T. Characterization of the dynamic growth of the nanobubble within the confined glass nanopore. *Anal. Chem.* **2018**, *90* (21), 12352−12355.
(25) Ying, Y.-L.; Hu, Y.-X.; Gao, R.; Yu, R.-J.; Gu, Z.; Lee, L. P.; Long, Y.-T. Asymmetric nanopore electrode-based amplification for electron transfer imaging in live cells. *J. Am. Chem. Soc.* **2018**, *140* (16), 5385−5392.
(26) Jia, X.; Wang, E.; Wang, J. Rational design of nanozymes for engineered cascade catalytic cancer therapy. *Chem. Rev.* **2025**, *125* (5), 2908−2952.
(27) Zhou, H.; Zhang, Y.; Wang, S.; Gao, Z.; Zhao, C.; Song, P.; Li, X.; Song, Y.-Y. Engineering a pH-responsive Fabry−Pérot interferometer for real-time glucose sensing. *Chin. Chem. Lett.* **2025**, No. 111643.
(28) Sun, D.-W.; Huang, L.; Pu, H.; Ma, J. Introducing reticular chemistry into agrochemistry. *Chem. Soc. Rev.* **2021**, *50* (2), 1070−1110.
(29) Ai, Y.; Sun, H.; Gao, Z.; Wang, C.; Guan, L.; Wang, Y.; Wang, Y.; Zhang, H.; Liang, Q. Dual enzyme mimics based on metal−ligand cross-linking strategy for accelerating ascorbate oxidation and enhancing tumor therapy. *Adv. Funct. Mater.* **2021**, *31* (40), No. 2103581.
(30) Li, S.; Shang, L.; Xu, B.; Wang, S.; Gu, K.; Wu, Q.; Sun, Y.; Zhang, Q.; Yang, H.; Zhang, F.; et al. A nanozyme with photo-enhanced dual enzyme-like activities for deep pancreatic cancer therapy. *Angew. Chem., Int. Ed.* **2019**, *58* (36), 12624−12631.
(31) Huang, Y.; Ren, J.; Qu, X. Nanozymes: Classification, catalytic mechanisms, activity regulation, and applications. *Chem. Rev.* **2019**, *119* (6), 4357−4412.
(32) Liu, Y.; Cheng, Y.; Zhang, H.; Zhou, M.; Yu, Y.; Lin, S.; Jiang, B.; Zhao, X.; Miao, L.; Wei, C.-W.; et al. Integrated cascade nanozyme catalyzes in vivo ros scavenging for anti-inflammatory therapy. *Sci. Adv.* **2020**, *6* (29), No. eabb2695.
(33) Ozkan, S.; Nguyen, N. T.; Mazare, A.; Cerri, I.; Schmuki, P. Controlled spacing of self-organized anodic TiO_2 nanotubes. *Electrochem. Commun.* **2016**, *69*, 76−79.
(34) Sun, Z.; Gu, Z.; Ma, W. Confined electrochemical behaviors of single platinum nanoparticles revealing ultrahigh density of gas molecules inside a nanobubble. *Anal. Chem.* **2023**, *95* (7), 3613−3620.
(35) Guo, J.; Liu, X.; Zhao, J.; Xu, H.; Gao, Z.; Wu, Z.-Q.; Song, Y.-Y. Rational design of mesoporous chiral mofs as reactive pockets in nanochannels for enzyme-free identification of monosaccharide enantiomers. *Chem. Sci.* **2023**, *14* (7), 1742−1751.
(36) Xu, Y.; Zhao, C.; Zhang, X.; Xu, J.; Yang, L.; Zhang, Z.; Gao, Z.; Song, Y.-Y. Engineering tailorable TiO_2 nanotubes for nir-controlled drug delivery. *Nano Res.* **2021**, *14* (11), 4046−4055.
(37) Lu, H.; Zhong, J.; Ji, C.; Zhao, J.; Li, D.; Zhao, R.; Jiang, Y.; Fang, S.; Liang, T.; Li, H.; Li, C. M. Fabricating an optimal rutile TiO_2 electron transport layer by delicately tuning ticl4 precursor solution for high performance perovskite solar cells. *Nano Energy* **2020**, *68*, No. 104336.
(38) Chen, Q.; Luo, L.; Faraji, H.; Feldberg, S. W.; White, H. S. Electrochemical measurements of single H_2 nanobubble nucleation and stability at pt nanoelectrodes. *J. Phys. Chem. Lett.* **2014**, *5* (20), 3539−3544.
(39) Edwards, M. A.; Robinson, D. A.; Ren, H.; Cheyne, C. G.; Tan, C. S.; White, H. S. Nanoscale electrochemical kinetics & dynamics: The challenges and opportunities of single-entity measurements. *Faraday Discuss.* **2018**, *210* (0), 9−28.
(40) Tian, L.; Liang, J.; Gao, Y.; Gao, X.; Kang, X. Current oscillations from bipolar nanopores for statistical monitoring of hydrogen evolution on a confined electrochemical catalyst. *Phys. Chem. Chem. Phys.* **2023**, *25* (11), 7629−7633.
(41) Tseng, W. J.; Wu, P.-S. Effect of sodium dodecul sulfate on stability of gibbsite platelet stabilized emulsion foams. *Ceram. Int.* **2012**, *38* (4), 2711−2718.
(42) Liu, W.; Yang, C.-N.; Yang, Z.-L.; Yu, R.-J.; Long, Y.-T.; Ying, Y.-L. Observing confined local oxygen-induced reversible thiol/disulfide cycle with a protein nanopore. *Angew. Chem., Int. Ed.* **2023**, *62* (27), No. e202304023.
(43) Chen, J.; Ma, Q.; Li, M.; Chao, D.; Huang, L.; Wu, W.; Fang, Y.; Dong, S. Glucose-oxidase like catalytic mechanism of noble metal nanozymes. *Nat. Commun.* **2021**, *12* (1), No. 3375.
(44) Shen, X.; Wang, Z.; Gao, X. J.; Gao, X. Reaction mechanisms and kinetics of nanozymes: Insights from theory and computation. *Adv. Mater.* **2024**, *36* (10), No. 2211151.
(45) Nosaka, Y.; Nosaka, A. Y. Generation and detection of reactive oxygen species in photocatalysis. *Chem. Rev.* **2017**, *117* (17), 11302−11336.
(46) Zhao, X.; Yang, T.; Wang, D.; Zhang, N.; Yang, H.; Jing, X.; Niu, R.; Yang, Z.; Xie, Y.; Meng, L. Gold nanorods/metal−organic framework hybrids: Photo-enhanced peroxidase-like activity and sers performance for organic dyestuff degradation and detection. *Anal. Chem.* **2022**, *94* (10), 4484−4494.
(47) Wang, F.; Wong, R. J.; Ho, J. H.; Jiang, Y.; Amal, R. Sensitization of pt/tio2 using plasmonic au nanoparticles for hydrogen evolution under visible-light irradiation. *ACS Appl. Mater. Interfaces* **2017**, *9* (36), 30575−30582.

https://doi.org/10.1021/acscatal.6c00460
ACS Catal. 2026, 16, 7611−7618